

## Auto-calibration of Automotive Radars in Operational Mode Using Simultaneous Localisation and Mapping

Petrov, Nikita; Krasnov, Oleg; Yarovoy, Alexander

**DOI**

[10.1109/TVT.2021.3058778](https://doi.org/10.1109/TVT.2021.3058778)

**Publication date**

2021

**Document Version**

Final published version

**Published in**

IEEE Transactions on Vehicular Technology

**Citation (APA)**

Petrov, N., Krasnov, O., & Yarovoy, A. (2021). Auto-calibration of Automotive Radars in Operational Mode Using Simultaneous Localisation and Mapping. *IEEE Transactions on Vehicular Technology*, 70(3), 2062-2075. Article 9353252. <https://doi.org/10.1109/TVT.2021.3058778>

**Important note**

To cite this publication, please use the final published version (if applicable). Please check the document version above.

**Copyright**

Other than for strictly personal use, it is not permitted to download, forward or distribute the text or part of it, without the consent of the author(s) and/or copyright holder(s), unless the work is under an open content license such as Creative Commons.

**Takedown policy**

Please contact us and provide details if you believe this document breaches copyrights. We will remove access to the work immediately and investigate your claim.

***Green Open Access added to TU Delft Institutional Repository***

***'You share, we take care!' - Taverne project***

**<https://www.openaccess.nl/en/you-share-we-take-care>**

Otherwise as indicated in the copyright section: the publisher is the copyright holder of this work and the author uses the Dutch legislation to make this work public.

# Auto-Calibration of Automotive Radars in Operational Mode Using Simultaneous Localisation and Mapping

Nikita Petrov<sup>1</sup>, Oleg Krasnov<sup>1</sup>, and Alexander G. Yarovoy, *Fellow, IEEE*

**Abstract**—This paper presents an analysis of a new method of automotive radar self-calibration which uses targets of opportunity. While conventional offline calibration of a phased array antenna requires accurate knowledge of the positions of calibration targets relative to the radar, such information is not available in a dynamic scenario. To compensate for this, we have developed an estimation procedure based on an extended Kalman filter (EKF) to address the challenge of simultaneous localisation, mapping and calibration. The proposed technique makes it possible to compensate for moderate errors of amplitude and phase in the phased array response with just a few measured frames. A significant reduction in the sidelobe rejection of the array response, plus the ability to correct for angular steering errors, are demonstrated via numerical simulations and real data processing.

**Index Terms**—Calibration, phased arrays, radar, SLAM.

## I. INTRODUCTION

THE realisation of self-driving cars considerably depends upon the availability of high-resolution sensors to perceive information about the surrounding space. Modern design of highly autonomous car control relies on the joint processing of data collected by three types of sensors: camera, lidar and mm-wave radar. Optical and laser sensors have an advantage over radar in terms of angular resolution and information capacity, while the relevance of radar comes from its robustness under varying weather and light conditions, together with its ability to measure the radial velocity of the surrounding scene and to “look” around objects (by multi-path propagation of radio waves) [1]. Modern automotive radars have instantaneous large-angle coverage, achieved by using multiple-input, multiple-output (MIMO) radar systems in combination with high-resolution spectrum techniques such as multiple signal decomposition (MUSIC). These techniques are very sensitive to calibration errors. Therefore, the proper calibration of antenna arrays is vital to the performance of automotive radars.

Manuscript received June 12, 2020; revised October 27, 2020 and January 14, 2021; accepted February 4, 2021. Date of publication February 11, 2021; date of current version April 2, 2021. This work was partly supported by NWO TTW under Project STW #13563: “Standardized Self-Diagnostic Sensing Systems for Highly Automated Driving.” The review of this article was coordinated by Dr. Hai Lin. (*Corresponding author: Nikita Petrov.*)

The authors are with the Microwave Sensing, Signals and Systems (MS3), Delft University of Technology, Delft 2628, the Netherlands (e-mail: n.petrov@tudelft.nl; O.A.Krasnov@tudelft.nl; A.Yarovoy@tudelft.nl).

Digital Object Identifier 10.1109/TVT.2021.3058778

With the development of the first phased array radar, array calibration became a crucial task in the production and maintenance of radars. Array calibration is a procedure that corrects hardware imperfections such as gain, phase, array element locations, mutual coupling between elements and I/Q imbalance [2]. Similarly to the presence of noise, clutter and interference in the data, calibration errors degrade radar performance, particularly the accuracy and target response of (high-resolution) direction-of-arrival (DOA) estimation techniques [3]–[5], interference cancellation [6] and target detection. Calibration remains a limiting factor in MIMO arrays, which have replaced conventional phased arrays in modern automotive radars.

There are two general approaches to antenna calibration. In the “naive” approach, array measurements are collected in a controlled environment, e.g. in an anechoic chamber with corner reflectors installed at predefined locations. An alternative approach, known as “auto-calibration,” is to perform the radar calibration in operational mode using sources at unknown locations [2]. Controlled calibration benefits from the ability to measure and compensate for errors of any type, whereas auto-calibration can correct for only a restricted class of errors, determined by the finite number of parameters available within the model [7], [8]. On the other hand, because auto-calibration is performed simultaneously with the data collection, the changes in array parameters due to external factors such as temperature, humidity, aging, etc. can be compensated. This functionality is crucial for reliable sensor operation under changing conditions.

In parametric calibration methods, array distortion is modelled with a set of estimated parameters. Examples of these parameters are: errors in the location, gain or phase of the array elements; mutual coupling matrices; and I/Q channel imbalances. Parametric calibration methods are typically global, meaning that the same calibration coefficients are independently applied to beamforming in any direction. In local calibration methods, different calibration coefficients are applied to beamforming in different directions. One way to realise this is to measure array response at several fixed locations and interpolate calibration coefficients to arbitrary steering directions. This is known as interpolation of calibration data [2], [9].

Many auto-calibration methods developed to date are based either on an extension of the MUSIC algorithm [7] or on the maximum likelihood approach [8], [10]. The difficulty of identifying parameters for auto-calibration has been addressed in [11]–[13]. An overview and comparative analysis of the most

popular calibration techniques can be found in [2], [14]. The key step in all of these techniques is estimating the signal covariance matrix, which requires the availability of a sufficient number of independent data samples (snapshots). It assumes a constant bearing of the measured targets over the observation time, yet this can hardly be satisfied with an automotive radar moving on the road. Non-negligible displacement of the car within the data collection time implies variation in the targets' angular locations and the smearing of the MUSIC spectrum. This displacement can either be compensated [15] or targets can be tracked before calibration [16].

The problem is significantly simplified if the locations of the sources are known and/or the array parameters affect array response linearly. In such a case the calibration problem is formulated with a linear data model and a simple yet efficient solution is derived via the least-squares fit. Two special approaches are of practical interest and are commonly used: estimation of the full calibration matrix with coupling [17], [18]; and the estimation of its diagonal, accounting for channel errors only [17], [19]. The latter approach is widely used in MIMO systems with sparse array(s).

The growing field of automotive radars operating in mm-waves (24 GHz, 77 GHz, 79 GHz bands) reveals the challenges surrounding the development and maintenance of low-cost phased arrays, including how to accomplish frequent calibration. Calibration of automotive radars has recently attracted widespread interest [20], [21]. A closely related line of research is devoted to the extrinsic calibration of multiple sensors mounted on the car, e.g. [22]. This calibration is, however, still performed only during regular maintenance checks of the car, see [23], [24].

The problem with radar calibration in operational mode has been investigated, but no solutions have been raised. In this paper we propose a method for forward-looking automotive radar auto-calibration in operational mode. We use some principles of simultaneous localisation and mapping (SLAM) as a tool to extract the location of the sensor and the targets (hereinafter called landmarks) in the scene, necessary for proper array calibration. After formulating the problem of simultaneous localisation, mapping and calibration, we present an efficient solution for online sensor calibration in a dense target environment.

The structure of this paper is as follows: in Section II we utilise the least-squares method for array calibration and demonstrate its dependence on the knowledge of target (landmark) locations. Next, in Section III we look at SLAM using radar measurements and at its solution with the extended Kalman filter (EKF). The problem of simultaneous localisation, calibration and mapping is introduced in Section IV and solved with EKF. Simulation results are further presented in Section V, demonstrating the feasibility of the concept of joint SLAM and calibration. It is shown that only a few measurements are required to obtain a reliable estimation of the calibration coefficients. The application of the proposed approach to a real data set is presented in Section VI. Finally, the conclusion is drawn in Section VII.

*Notations:* Hereinafter we use lowercase boldface letters for vectors, uppercase boldface letters for matrices, and uppercase boldface calligraphic letters for sets. The superscripts  $(\cdot)^T$ ,  $(\cdot)^H$

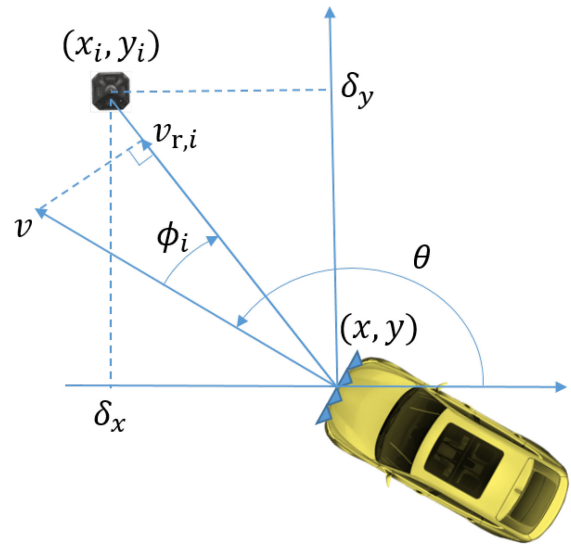


Fig. 1. Measurement geometry with the observed landmark at  $(x_i, y_i)$ , note that  $\phi_i < 0$ .

and  $(\cdot)^*$  indicate matrix/vector transpose, Hermitian transpose and complex conjugate, respectively.

## II. LEAST SQUARES CALIBRATION OF ANTENNA ARRAY

The least squares calibration is commonly used for its simplicity and robustness to different types of calibration errors, including the coupling terms. To overcome the need for absolute magnitude and phase measurement, relative measurements between the channels are often employed, which allows us to remove range and target dependence from the calibration problem [2], [18]. Modern automotive radars use coherent MIMO arrays for DOA estimation. The employed virtual arrays benefit from the smaller coupling between adjacent array elements due to the sparse structure of the transmitting antenna (or receiving antenna, or both), and thus calibration can be done over the gain and the phase only [19].

Consider a virtual uniform linear array (ULA) of  $M$  elements observing a point-like target at angle  $\phi_i$  from the array pointing direction, see Fig. (1). The target is characterised by its complex back-scattering coefficient  $\alpha_i = |\alpha_i|e^{j\varphi_i}$  with  $\varphi_i \sim \mathcal{U}(0, 2\pi)$ , which comprises signal attenuation due to two-way propagation and processing gain with no loss of generality. The amplitude and phase distortion in the  $m$ -th element of the array is characterised by a complex-valued coefficient  $\gamma_m$ ,  $m = 0, \dots, M - 1$ . Then, the response of the  $i$ -th target in the  $m$ -th antenna element  $\kappa_{m,i}$  is given by:

$$\kappa_{m,i} = \alpha_i \gamma_m \exp\left(-j2\pi \frac{dm}{\lambda} \sin(\phi_i)\right) + n_{m,i}, \quad (1)$$

where  $\lambda$  stands for the carrier wavelength,  $d$  is the inter-element spacing of the ULA and  $n_{m,i} \sim (0, \sigma_n^2)$  represents the receiver noise.

To remedy the dependence on the target back-scattering coefficient  $\alpha_i$ , we consider channel  $m = 0$  (another  $m$  can be used with no loss of generality) as the reference point. This implies

that the calibration coefficient at  $\gamma_0 = 1$  is fixed. The new data set  $\mathbf{P} \in \mathbb{C}^{(M-1) \times N_i}$  is obtained by normalising the target response in every channel via:

$$p_{m,i} = \frac{\kappa_{m,i}}{\kappa_{0,i}} = \gamma_m \exp\left(-j2\pi \frac{dm}{\lambda} \sin(\phi_i)\right) + n'_{m,i}. \quad (2)$$

The receiver noise being defined by  $n_{m,i} \sim (0, \sigma_n^2)$  implies

$$n'_{m,i} \sim \left(0, \frac{\sigma_n^2}{\alpha_i^2 + \sigma_n^2}\right) \quad (3)$$

and thus depends on the target SNR:

$$\text{SNR} = \frac{\alpha_i^2}{\sigma_n^2}. \quad (4)$$

Note that normalisation by a constant in (2) does not affect target SNR nor its DOA estimation.

To perform calibration in a stationary scenario we collect the normalised responses of all the observed targets  $\mathbf{P}$  and compare them to the expected array response in the same channel. For the calibration we assume that the angles of all observed targets  $\phi_i, i = 1, \dots, N_i$  are known, and we use them to form the steering vectors for the corresponding targets in matrix  $\mathbf{H} \in \mathbb{C}^{(M-1) \times N_i}$  with elements:

$$h_{m,i} = \exp\left(-j2\pi \frac{dm}{\lambda} \sin(\phi_i)\right). \quad (5)$$

The calibration coefficients  $\boldsymbol{\gamma} = [\gamma_1, \dots, \gamma_{M-1}]^T$  are then estimated by the least squares method:

$$\gamma_m = \frac{\sum_i^{N_i} h_{m,i} p_{m,i}^*}{\sum_i^{N_i} |p_{m,i}|^2}, \quad m = 1, \dots, M-1. \quad (6)$$

The accuracy of the calibration depends on the SNR and the number of available observations. In reality, the angles of the targets are not perfectly known, which affects the calibration accuracy. Moreover, new measurements are created because of the movement of the platform and are thus not immediately available to the radar.

The choice of the coupling-free model in this study is motivated by several factors:

- 1) The solution of (6) exists even with one observation [17];
- 2) Least squares estimation (6) with independent observations can be calculated sequentially [25]; and
- 3) Calibration (6) is stable against small angular errors of the measured targets.

These features of the least squares calibration will be exploited in Section IV.

### III. SIMULTANEOUS LOCALISATION AND MAPPING WITH RADAR MEASUREMENTS

#### A. Probabilistic Formulations of SLAM

The objective of simultaneous localisation and mapping (SLAM) is to provide a joint estimation of vehicle location and orientation parameters,<sup>1</sup> together with the map of surrounding

<sup>1</sup>In this study we assume that vehicle location corresponds to the radar location.

objects at each time instant  $t = 0, \dots, N_t$ . Vehicle location  $(x, y)$ , orientation  $\theta$  and instantaneous velocity  $v$  form the state vector  $\mathbf{x}^{[t]} = [x, y, \theta, v]^T$ .<sup>2</sup> The map, assumed stationary, consists of  $N$  landmarks with locations  $\mathbf{m} = [x_1, y_1, \dots, x_N, y_N]^T$ . The online SLAM, considered herein, aims to estimate the current position of the sensor (at time instant  $t$  only, rather than the whole trajectory) and thus implies a dynamic estimation of  $2N + 4$  parameters  $\mathbf{s}^{[t]} = [x, y, \theta, v, x_1, y_1, \dots, x_N, y_N]^T$ .

The conventional description of the SLAM problem is provided in a probabilistic way [26]–[29]. At every time step  $t$  SLAM computes the joint distribution of the sensor location and the map:

$$P\left(\mathbf{x}^{[t]}, \mathbf{m} | \mathcal{Z}^{[0:t]}, \mathbf{U}^{[0:t]}, \mathbf{x}^{[0]}\right), \quad (7)$$

where the set  $\mathcal{Z}^{[0:t]} = \{\mathbf{z}^{[0]}, \dots, \mathbf{z}^{[t]}\}$  combines the measurements of all detected targets until time  $t$ , the control inputs to the platform are given via  $\mathbf{U}^{[0:t]} = \{\mathbf{u}^{[0]}, \dots, \mathbf{u}^{[t]}\}$ , and  $\mathbf{x}^{[0]}$  is the initial position of the platform. The solution is based on the observation (measurement) and dynamic (motion) models, defined respectively as:

$$P(\mathbf{z}^{[t]} | \mathbf{x}^{[t]}, \mathbf{m}), \quad (8)$$

$$P(\mathbf{x}^{[t]} | \mathbf{x}^{[t-1]}, \mathbf{u}^{[t]}). \quad (9)$$

The observation model calculates the probability of making the observation  $\mathbf{z}^{[t]}$  for the given sensor and landmarks locations. The motion model describes sensor motion in terms of the state transition.

The Bayesian recursive (sequential) filter provides the solution to the SLAM problem by applying the following prediction (time update) steps:

$$P\left(\mathbf{x}^{[t]}, \mathbf{m} | \mathcal{Z}^{[0:t-1]}, \mathbf{U}^{[0:t]}, \mathbf{x}^{[0]}\right) = \int P\left(\mathbf{x}^{[t]} | \mathbf{x}^{[t-1]}, \mathbf{u}^{[t]}\right) \cdot P\left(\mathbf{x}^{[t-1]}, \mathbf{m} | \mathcal{Z}^{[0:t-1]}, \mathbf{U}^{[0:t-1]}, \mathbf{x}^{[0]}\right) d\mathbf{x}^{[t-1]} \quad (10)$$

and correction (measurement update) steps:

$$P\left(\mathbf{x}^{[t]}, \mathbf{m} | \mathcal{Z}^{[0:t]}, \mathbf{U}^{[0:t]}, \mathbf{x}^{[0]}\right) = \frac{P(\mathbf{z}^{[t]} | \mathbf{x}^{[t]}, \mathbf{m}) P(\mathbf{x}^{[t]}, \mathbf{m} | \mathcal{Z}^{[0:t-1]}, \mathbf{U}^{[0:t]}, \mathbf{x}^{[0]})}{P(\mathbf{z}^{[t]} | \mathcal{Z}^{[0:t-1]}, \mathbf{U}^{[0:t]})}. \quad (11)$$

The output represents the statistical description of the sensor location  $\mathbf{x}^{[t]}$  and the map  $\mathbf{m}$ . Recall that herein we assume no measurement error induced by sensor calibration.

In this paper we focus on filter-based SLAM, which describes the map with a set of landmarks (targets). We demonstrate the applicability of continuous calibration with EKF SLAM. In general, calibration can be incorporated in other types of feature-based SLAM in a similar manner.

#### B. SLAM With Radar Measurements

The classical SLAM problem is formulated for the laser sensor, which provides the range and angular measurements

<sup>2</sup>For simplicity of notations we have skipped the time dependence for scalar variables.

of surrounding objects [28]. Conventional radar systems provide accurate velocity measurement through Doppler processing (hereinafter we assume that no velocity ambiguities occur), but they typically have poorer angular and range resolution than lidars. Here we assume that no calibration errors occur. The geometry of the problem is described in Fig. 1 for a single target observation. At time  $t$  the radar measures the range, angle and radial (Doppler) velocity of every observed target:  $\mathbf{z}_i = [r_i, \phi_i, v_{r,i}]^T$  and stores the measurements of  $N$  observed landmarks in a vector:  $\mathbf{z}^{[t]} = [\mathbf{z}_{i_1}^T, \dots, \mathbf{z}_{i_N}^T]^T$ . We assume that the data association problem is resolved and that every measurement corresponds to the proper landmark in the map with index  $i$ .

The measurement model is given by the nonlinear function:

$$\mathbf{z}^{[t]} = \mathbf{g}^{[t]}(\mathbf{s}^{[t]}) + \boldsymbol{\omega}^{[t]}, \quad (12)$$

where  $\mathbf{s}^{[t]} = [\mathbf{x}^{[t]}, \mathbf{m}]^T$  is the state vector. The function  $\mathbf{g}^{[t]}(\mathbf{s}^{[t]})$  is determined according to radar principles and geometry for the  $i$ -th target, presented in Fig. 1, via:

$$\begin{aligned} r_i &= \sqrt{(x_i - x)^2 + (y_i - y)^2}; \\ \phi_i &= \text{atan2}(y_i - y, x_i - x) - \theta; \\ v_{r,i} &= v \cos(\text{atan2}(y_i - y, x_i - x) - \theta), \end{aligned} \quad (13)$$

where  $\text{atan2}(y, x)$  evaluates the angle of the vector in the Euclidean plane, given its coordinates  $(x, y)$ . It can be alternatively defined as the principal value of the argument function  $\text{atan2}(y, x) = \text{Arg}(x + jy)$  in the interval  $(-\pi, \pi]$ .

If we assume that every measurement is associated with one landmark, independent of the other map, and if we define the following notations for the  $i$ -th landmark:

$$\begin{aligned} \delta_x &= x_i - x; \\ \delta_y &= y_i - y; \\ q &= (x_i - x)^2 + (y_i - y)^2, \end{aligned} \quad (14)$$

then the function  $\mathbf{g}^{[t]}(\mathbf{s}^{[t]})$  defined in (13) can be partitioned for each landmark by  $\mathbf{g}_i^{[t]}(\mathbf{s}_i^{[t]})$  and linearised by its first-order Taylor expansion around its prediction  $\bar{\mathbf{s}}_i^{[t]}$  as:

$$\mathbf{g}_i^{[t]}(\mathbf{s}_i^{[t]}) \approx \mathbf{g}_i^{[t]}(\bar{\mathbf{s}}_i^{[t]}) + \mathbf{G}_i^{[t]}(\mathbf{s}_i^{[t]} - \bar{\mathbf{s}}_i^{[t]}), \quad (15)$$

where the state sub-vector  $\mathbf{s}_i^{[t]} = [x, y, \theta, v, x_i, y_i]^T$  is considered and the measurements are represented by  $\mathbf{z}_i^{[t]} = [r_i, \phi_i, v_{r,i}]^T$ . The corresponding Jacobian of the form:

$$\mathbf{G}_i^{[t]} = \left. \frac{\partial \mathbf{g}_i^{[t]}}{\partial \mathbf{s}_i^{[t]}} \right|_{\mathbf{s}_i^{[t]} = \bar{\mathbf{s}}_i^{[t]}} = [\mathbf{G}_{i,x}^{[t]}, \mathbf{G}_{i,m}^{[t]}] \quad (16)$$

can be partitioned into the submatrix  $\mathbf{G}_{i,x}^{[t]} \in \mathbb{R}^{3 \times 4}$  for sensor location variables  $\mathbf{x}^{[t]}$ :

$$\mathbf{G}_{i,x}^{[t]} = \frac{1}{q} \begin{bmatrix} -\sqrt{q}\delta_x & -\sqrt{q}\delta_y & 0 & 0 \\ \delta_y & -\delta_x & -q & 0 \\ -v \sin(\phi_i)\delta_y & v \sin(\phi_i)\delta_x & v \sin(\phi_i)q & \cos(\phi_i) \end{bmatrix} \quad (17)$$

and submatrix  $\mathbf{G}_{i,m}^{[t]} \in \mathbb{R}^{3 \times 2}$  for the map (landmark location):

$$\mathbf{G}_{i,m}^{[t]} = \frac{1}{q} \begin{bmatrix} \sqrt{q}\delta_x & \sqrt{q}\delta_y \\ -\delta_y & \delta_x \\ v \sin(\phi_i)\delta_y & -v \sin(\phi_i)\delta_x \end{bmatrix}. \quad (18)$$

Every measurement is then associated with an existing landmark, or a new landmark is created. All of the measurements associated with existing landmarks form the measurement vector  $\mathbf{z}^{[t]}$ , and the Jacobian matrix  $\mathbf{G}^{[t]}$  is built from the corresponding blocks  $\mathbf{G}_i^{[t]}$  as e.g. in [28]. Then the update step of EKF can be done via:

$$\mathbf{K}^{[t]} = \bar{\mathbf{M}}^{[t]} \mathbf{G}^{[t]T} (\mathbf{G}^{[t]} \bar{\mathbf{M}}^{[t]} \mathbf{G}^{[t]T} + \mathbf{R}^{[t]})^{-1}; \quad (19)$$

$$\hat{\mathbf{s}}^{[t]} = \bar{\mathbf{s}}^{[t]} + \mathbf{K}^{[t]} (\mathbf{z}^{[t]} - \mathbf{g}^{[t]}(\bar{\mathbf{s}}^{[t]})); \quad (20)$$

$$\hat{\mathbf{M}}^{[t]} = (\mathbf{I} - \mathbf{K}^{[t]} \mathbf{G}^{[t]}) \bar{\mathbf{M}}^{[t]}, \quad (21)$$

where  $\mathbf{R}^{[t]} = \text{diag}[\mathbf{R}_1^{[t]}, \dots, \mathbf{R}_N^{[t]}]$  is the block-diagonal measurement covariance matrix for  $N$  observations at time instant  $t$ , with the  $i$ -th block being defined as  $\mathbf{R}_i^{[t]} = \text{diag}[\sigma_{r,i}^{[t]2}, \sigma_{\phi,i}^{[t]2}, \sigma_{v,i}^{[t]2}]$ . Recall that the SNR of a target varies with the distance to it.

The dynamic model describes the movement of the platform and landmarks in time:  $\mathbf{s}^{[t]} = \mathbf{a}^{[t]}(\mathbf{s}^{[t-1]}) + \mathbf{u}^{[t]}$ . The landmarks are assumed stationary, as in most of SLAM literature [26]–[29]. The nearly constant velocity model is assumed for platform movement here:

$$\begin{aligned} x^{[t]} &= x^{[t-1]} + Tv^{[t-1]} \cos(\theta^{[t-1]}); \\ y^{[t]} &= y^{[t-1]} + Tv^{[t-1]} \sin(\theta^{[t-1]}); \\ \theta^{[t]} &= \theta^{[t-1]} + u_{\theta}^{[t]}; \\ v^{[t]} &= v^{[t-1]} + u_v^{[t]}, \end{aligned} \quad (22)$$

where  $T$  is the time interval between the measurements and  $u_{\theta}^{[t]} \sim \mathcal{N}(0, \sigma_{\theta}^2)$  and  $u_v^{[t]} \sim \mathcal{N}(0, \sigma_v^2)$  define the driving noise of bearing and velocity.

The prediction step is done via:

$$\bar{\mathbf{s}}^{[t]} = \mathbf{a}^{[t]}(\hat{\mathbf{s}}^{[t-1]}); \quad (23)$$

$$\bar{\mathbf{M}}^{[t]} = \mathbf{A}^{[t-1]} \hat{\mathbf{M}}^{[t-1]} \mathbf{A}^{[t-1]T} + \mathbf{Q}, \quad (24)$$

where  $\mathbf{Q}$  describes a priori known uncertainty of the dynamic model and  $\mathbf{A}^{[t]} = \left. \frac{\partial \mathbf{a}^{[t]}}{\partial \mathbf{s}^{[t]}} \right|_{\mathbf{s}^{[t]} = \bar{\mathbf{s}}^{[t-1]}}$  is the Jacobian of the dynamic model (22).

#### IV. JOINT LOCALISATION, MAPPING AND SENSOR CALIBRATION

##### A. Problem Statement

The calibration of the phased array requires information about the sensor and landmark locations in order to form the expected target response (5). In the general case of a moving platform,

calibration problem can be alternatively formulated in a probabilistic way:

$$P\left(\boldsymbol{\gamma}^{[t]}|\boldsymbol{z}^{[0:t]}, \boldsymbol{\mathcal{X}}^{[0:t]}, \mathbf{m}\right), \quad (25)$$

which implies that in order to estimate the calibration vector  $\boldsymbol{\gamma}^{[t]}$ , the radar location  $\boldsymbol{\mathcal{X}}^{[0:t]} = \{\mathbf{x}^{[0]}, \dots, \mathbf{x}^{[t]}\}$  and the map  $\mathbf{m}$  should be known for every measurement  $\boldsymbol{z}^{[0:t]} = \{\mathbf{z}^{[0]}, \dots, \mathbf{z}^{[t]}\}$ . This motivates the joint formulation of sensor self-calibration with SLAM. The joint solution should also benefit SLAM, because angular measurements with antenna array depend on the calibration coefficients. Poor calibration leads to additional beam-pointing error [3], undesirable for SLAM.

Combining (25) with the statistical definition of SLAM (7), we aim to estimate at each time step  $t$  the probability:

$$P\left(\mathbf{x}^{[t]}, \boldsymbol{\gamma}^{[t]}, \mathbf{m}|\boldsymbol{z}^{[0:t]}, \boldsymbol{\mathcal{U}}^{[0:t]}, \mathbf{x}^{[0]}\right), \quad (26)$$

which describes the problem of joint localisation –  $\mathbf{x}^{[t]}$ , calibration –  $\boldsymbol{\gamma}^{[t]}$  and mapping –  $\mathbf{m}$ . This probability can be calculated via a recursive Bayesian filter, similarly to the original SLAM problem (10), (11). It consists of the prediction step:

$$\begin{aligned} & P\left(\mathbf{x}^{[t]}, \boldsymbol{\gamma}^{[t]}, \mathbf{m}|\boldsymbol{z}^{[0:t-1]}, \boldsymbol{\mathcal{U}}^{[0:t]}, \mathbf{x}^{[0]}\right) \\ &= \iint P\left(\mathbf{x}^{[t]}|\mathbf{x}^{[t-1]}, \mathbf{u}^{[t]}\right) P\left(\boldsymbol{\gamma}^{[t]}|\boldsymbol{\gamma}^{[t-1]}\right) \\ &\cdot P\left(\mathbf{x}^{[t-1]}, \boldsymbol{\gamma}^{[t-1]}, \mathbf{m}|\boldsymbol{z}^{[0:t-1]}, \boldsymbol{\mathcal{U}}^{[0:t-1]}, \mathbf{x}^{[0]}\right) d\mathbf{x}^{[t-1]} d\boldsymbol{\gamma}^{[t-1]}; \end{aligned} \quad (27)$$

and the correction step:

$$\begin{aligned} & P\left(\mathbf{x}^{[t]}, \boldsymbol{\gamma}^{[t]}, \mathbf{m}|\boldsymbol{z}^{[0:t]}, \boldsymbol{\mathcal{U}}^{[0:t]}, \mathbf{x}^{[0]}\right) \\ &= \frac{P\left(\mathbf{z}^{[t]}|\mathbf{x}^{[t]}, \boldsymbol{\gamma}^{[t]}, \mathbf{m}\right) P\left(\mathbf{x}^{[t]}, \boldsymbol{\gamma}^{[t]}, \mathbf{m}|\boldsymbol{z}^{[0:t-1]}, \boldsymbol{\mathcal{U}}^{[0:t]}, \mathbf{x}^{[0]}\right)}{P\left(\mathbf{z}^{[t]}|\boldsymbol{z}^{[0:t-1]}, \boldsymbol{\mathcal{U}}^{[0:t]}\right)}. \end{aligned} \quad (28)$$

The difference with (10) and (11) is the addition of the calibration coefficients  $\boldsymbol{\gamma} = [\gamma_1, \dots, \gamma_{M-1}]^T$  to the state vector. We assume that no external control is provided to the calibration vector, thus  $P(\boldsymbol{\gamma}^{[t]}|\boldsymbol{\gamma}^{[t-1]})$ . The platform dynamics are defined as  $P(\mathbf{x}^{[t]}|\mathbf{x}^{[t-1]}, \mathbf{u}^{[t]})$ , as in (10). The observation model is described by the term  $P(\mathbf{z}^{[t]}|\mathbf{x}^{[t]}, \boldsymbol{\gamma}^{[t]}, \mathbf{m})$ , which explicitly demonstrates the need for the joint solution of the problem.

Moreover, the observation model for the  $i$ -th target no longer includes the measured angle of the target, as it depends on the array calibration. Instead, it includes  $2(M-1)$  normalised array measurements, see (2):  $\mathbf{z}_i = [r_i, v_{r,i}, p_{1,i}^R, \dots, p_{M-1,i}^R, p_{1,i}^I, \dots, p_{M-1,i}^I]^T$ . Note that the complex measurements are represented by their real and imaginary parts, essential for the estimation routine (i.e., the state vector cannot include both real and complex parameters at the same time [30]). Thus, the modified state now has  $4 + 2(M-1) + 2N$  parameters, namely  $\mathbf{s}^{[t]} = [x, y, \theta, v, \gamma_1^R, \dots, \gamma_{M-1}^R, \gamma_1^I, \dots, \gamma_{M-1}^I, x_1, y_1, \dots, x_N, y_N]^T$ .

## B. Observation Model

Consider the geometry described in Fig. 1. At time  $t$  the radar observes  $N$  landmarks:  $\mathbf{z}^{[t]} = [\mathbf{z}_{i_1}^T, \dots, \mathbf{z}_{i_N}^T]^T$  with indexes  $\{i_1, \dots, i_N\}$  in the global map. We assume that the data association problem is correctly resolved. The observation vector of a point-like target  $\mathbf{z}_i = [r_i, v_{r,i}, p_{1,i}^R, \dots, p_{M-1,i}^R, p_{1,i}^I, \dots, p_{M-1,i}^I]^T$  depends on the actual sensor location  $\mathbf{x}^{[t]} = [x, y, \theta, v]^T$ , the calibration  $\boldsymbol{\gamma}^{[t]} = [\gamma_1^R, \dots, \gamma_{M-1}^R, \gamma_1^I, \dots, \gamma_{M-1}^I]^T$  and the  $i$ -th target location  $\mathbf{m}_i = [x_i, y_i]^T$ . The complex response of the  $i$ -th target in the  $m$ -th antenna element is:

$$p_{m,i} = \gamma_m \exp\left(-j2\pi m \frac{d}{\lambda} \sin(\phi_i)\right), \quad (29)$$

where

$$\phi_i = \text{atan2}(y_i - y, x_i - x) - \theta. \quad (30)$$

Note that measured angle  $\phi_i$  is not independent of the array response; therefore it is not a part of the observation vector here. However, we will use this notation hereinafter for the corresponding nonlinear transformation of the ground truth (for model description) and the corresponding state estimation.

The observation of the  $i$ -th target is given by  $2M$  vector:

$$\begin{aligned} r_i &= \sqrt{(x_i - x)^2 + (y_i - y)^2}; \\ v_{r,i} &= v \cos(\text{atan2}(y_i - y, x_i - x) - \theta); \\ p_{m,i}^R &= \gamma_m^R \cos(\psi_{m,i}) - \gamma_m^I \sin(\psi_{m,i}); \\ p_{m,i}^I &= \gamma_m^R \sin(\psi_{m,i}) + \gamma_m^I \cos(\psi_{m,i}), \end{aligned} \quad (31)$$

where  $m = 1, \dots, M-1$  and

$$\psi_{m,i} = -2\pi m \frac{d}{\lambda} \sin(\phi_i). \quad (32)$$

The relationships in (31) form the measurement model, which can be written as a nonlinear function of multiple variables  $\mathbf{g}_i^{[t]}(\mathbf{s}_i^{[t]})$ , similarly to (12).

The corresponding Jacobian for the  $i$ -th target measurement  $\mathbf{G}_i^{[t]} \in \mathbb{R}^{2M \times (2M+4)}$  has a block structure:

$$\mathbf{G}_i^{[t]} = \left. \frac{\partial \mathbf{g}_i^{[t]}}{\partial \mathbf{s}_i^{[t]}} \right|_{\mathbf{s}_i^{[t]} = \bar{\mathbf{s}}_i^{[t]}} = \begin{bmatrix} \mathbf{G}_{rv,x} & \mathbf{G}_{rv,\gamma} & \mathbf{G}_{rv,m} \\ \mathbf{G}_{ar,x} & \mathbf{G}_{ar,\gamma} & \mathbf{G}_{ar,m} \end{bmatrix}, \quad (33)$$

where we have skipped target  $i$  and time index  $t$  of submatrices for simplicity of notation. The first notation in subscript – rv and ar – defines the set of measurement equations from (31) to which the Jacobian is calculated: rv corresponds to range and velocity measurements, while ar refers to the array measurements. The second notation indicates the relevant part of the state vector: the sensor location  $\mathbf{x} = [x, y, \theta, v]^T$  – x, the calibration coefficients  $\boldsymbol{\gamma}$  –  $\gamma$  or the  $i$ -th landmark location  $\mathbf{m}_i = [x_i, y_i]^T$  – m. The partial derivatives of  $[r_i, v_{r,i}]^T$  in (31) over the platform location  $\mathbf{x}$  gives submatrix  $\mathbf{G}_{rv,x} \in \mathbb{R}^{2 \times 4}$ :

$$\begin{aligned} & \mathbf{G}_{rv,x} \\ &= \frac{1}{q} \begin{bmatrix} -\sqrt{q}\delta_x & -\sqrt{q}\delta_y & 0 & 0 \\ -v \sin(\phi_i)\delta_y & v \sin(\phi_i)\delta_x & v \sin(\phi_i)q & \cos(\phi_i) \end{bmatrix}. \end{aligned} \quad (34)$$

It can be noted that range and velocity measurements do not depend on the calibration coefficients, and thus  $\mathbf{G}_{\text{rv},\gamma} = \mathbf{0}_{2 \times 2(M-1)}$ . Finally, the part of the Jacobian that relates range/velocity measurements to the landmark location  $\mathbf{G}_{\text{rv},m} \in \mathbb{R}^{2 \times 2}$  is defined via:

$$\mathbf{G}_{\text{rv},m} = \frac{1}{q} \begin{bmatrix} \sqrt{q}\delta_x & \sqrt{q}\delta_y \\ v \sin(\phi_i)\delta_y & -v \sin(\phi_i)\delta_x \end{bmatrix}. \quad (35)$$

The submatrices of the Jacobian (33) which correspond to the array measurements (31) can be given in a compact form by noticing that location- and landmark-related state variables contribute to the array response  $p_{m,i}^R, p_{m,i}^I$  only via  $\psi_{m,i}$ , see (32)- (30). This leads to the expressions:

$$\begin{aligned} \frac{\partial p_{m,i}^R}{\partial \xi} &= (-\gamma_m^R \sin(\psi_{m,i}) - \gamma_m^I \cos(\psi_{m,i})) \frac{\partial \psi_{m,i}}{\partial \xi}; \\ \frac{\partial p_{m,i}^I}{\partial \xi} &= (\gamma_m^R \cos(\psi_{m,i}) - \gamma_m^I \sin(\psi_{m,i})) \frac{\partial \psi_{m,i}}{\partial \xi}, \end{aligned} \quad (36)$$

valid for the platform location- and landmark-related variables of the state vector:  $\xi \in \{\mathbf{x}, \mathbf{m}_i\} = \{x, y, \theta, v, x_i, y_i\}$ . The partial derivative of  $\psi_{m,i}$  over the platform location variables  $\mathbf{x}$  gives  $1 \times 4$  vector:

$$\frac{\partial \psi_{m,i}}{\partial \mathbf{x}} = -2\pi m \frac{d}{\lambda} \cos \psi_{m,i} \frac{1}{q} [\delta_y \quad -\delta_x \quad -q \quad 0]. \quad (37)$$

Finally, the block of Jacobian  $\mathbf{G}_{\text{ar},x} \in \mathbb{R}^{2(M-1) \times 4}$  is built by stacking  $M-1$  rows of (36) real measurements in channels  $m = 0, \dots, M-1$  and their counterparts for the imaginary data.

Next, we find the partial derivative of  $\psi_{m,i}$  over the landmark variables  $\mathbf{m}_i$ :

$$\frac{\partial \psi_{m,i}}{\partial \mathbf{m}_i} = -2\pi m \frac{d}{\lambda} \cos \psi_{m,i} \frac{1}{q} [-\delta_y \quad \delta_x] \quad (38)$$

and concatenate the vectors for the real measurements in channels  $m = 0, \dots, M-1$  from (36) with those of the imaginary data to construct submatrix  $\mathbf{G}_{\text{ar},m} \in \mathbb{R}^{2(M-1) \times 2}$  in the Jacobian (33).

The last block of the Jacobian (33) corresponds to the partial derivatives of the received data with respect to the calibration coefficients  $\mathbf{G}_{\text{ar},\gamma} \in \mathbb{R}^{2(M-1) \times 2(M-1)}$ , given by the block diagonal matrix:

$$\mathbf{G}_{\text{ar},\gamma} = \begin{bmatrix} \cos(\psi_{m,i})\mathbf{I}_{M-1} & -\sin(\psi_{m,i})\mathbf{I}_{M-1} \\ \sin(\psi_{m,i})\mathbf{I}_{M-1} & \cos(\psi_{m,i})\mathbf{I}_{M-1} \end{bmatrix}. \quad (39)$$

Finally, all of the measurements at time  $t$  associated with the targets form the vector  $\mathbf{z}^{[t]}$ , and the corresponding Jacobian matrix  $\mathbf{G}^{[t]}$  is built [28]. Recall that every observation of a landmark has measurement noise defined by (3) for the complex case. Therefore, the additive noise in the real and imaginary parts follows  $\omega_i \sim (0, \sigma_{p,i}^2)$ , where  $\sigma_{p,i}^2 = \frac{\sigma_n^2}{2(\sigma_i^2 + \sigma_n^2)}$ , and the measurement noise in (12) for joint SLAM and calibration is  $\boldsymbol{\omega} \sim \mathcal{N}(0, \mathbf{R})$ , with  $\mathbf{R}_i = \text{diag}(\sigma_r^2, \sigma_{vr}^2, \sigma_{p,i}^2 \mathbf{1}_{1 \times 2(M-1)})$ .

### C. Landmark Initialisation

When a landmark is observed for the first time, the state vector is amended by:

$$\begin{aligned} x_i &= x + r \cos(\theta + \hat{\phi}); \\ y_i &= y + r \sin(\theta + \hat{\phi}), \end{aligned} \quad (40)$$

where  $\hat{\phi}$  is the angle of arrival estimation based on the received data. If we assume that the map is sparse, such that only one landmark corresponds to every detection in the range/Doppler plane (the responses in multiple channels can be summed noncoherently to improve SNR at the detection stage), then the target angle of arrival is estimated as:

$$\hat{\phi}_i = \underset{\phi}{\text{argmax}} \frac{\mathbf{a}^H(\phi)\hat{\mathbf{\Gamma}}^{-1}\mathbf{p}_i}{\mathbf{a}^H(\phi)\mathbf{a}(\phi)}. \quad (41)$$

Here  $\hat{\mathbf{\Gamma}} = \text{diag}(\hat{\boldsymbol{\gamma}}) = \text{diag}(\hat{\gamma}_m^R + j\hat{\gamma}_m^I)$ ,  $m = 0, \dots, M-1$ , where  $\hat{\gamma}_0^R = 1$  and  $\hat{\gamma}_0^I = 0$  is the calibration matrix,  $\mathbf{p}_i = [1, p_{1,i}^R, \dots, p_{M-1,i}^R]^T + j[0, p_{1,i}^I, \dots, p_{M-1,i}^I]^T$  is the received signal from the  $i$ -th target and  $\mathbf{a}(\phi)$  is the array steering vector, as in (5).

If we assume a small and homogeneous calibration error over the aperture and a high target SNR, then the bearing estimation is approximately Gaussian with variance:

$$\sigma_{\phi}^2 = k_0 (\sigma_{\phi,\gamma}^2 + \sigma_{\phi,n}^2). \quad (42)$$

Here  $k_0 > 1$  is the scaling factor used to account for the degradation of the DOA estimation algorithm's accuracy from its Cramer-Rao bound (CRB) and  $\sigma_{\phi,\gamma}^2$  is the beam steering error induced by calibration error. From [3] this can be related to the variance of the calibration error:  $\sigma_{\gamma}^2 = \frac{1}{2(M-1)} \sum_{m=1}^M (\sigma_{\gamma,m}^R)^2 + (\sigma_{\gamma,m}^I)^2$ , where  $(\sigma_{\gamma,m}^R)^2$  and  $(\sigma_{\gamma,m}^I)^2$  are the diagonal elements of  $\mathbf{M}$  in EKF (19), via:

$$\sigma_{\phi,\gamma}^2 \approx \frac{3\sigma_{\gamma}^2\lambda^2}{\pi^2 d^2 \cos^2(\phi)(M-1)^3}. \quad (43)$$

Note that (43) is obtained using the relationship between the amplitude and phase errors of a complex Gaussian variable. The applicability of the approximation (43) is verified in Fig. 2. There, the variance and kurtosis of the bearing estimation as the functions of calibration error variance are shown, assuming  $\boldsymbol{\gamma} \sim \mathcal{N}(\mathbf{0}, \sigma_{\gamma}^2 \mathbf{I})$ . The results of  $10^4$  Monte-Carlo trials show that the approximation (43) is valid for  $\sigma_{\gamma}^2 \leq 0.16$ , or equivalently  $\sigma_{\gamma} \leq 0.4$ , for  $M = 12$ . For larger values of  $\sigma_{\gamma}^2$  the kurtosis grows, which implies non-Gaussian behavior in the beam-pointing error. This happens because the calibration error distorts the main lobe of the beamforming, leading to large deviations of the estimated bearing from the true one. This shows the limited applicability of the proposed auto-calibration algorithm and implies that preliminary array calibration in the factory/garage is still required.

The second term in (42) is the bearing estimation error due to the presence of noise. For high SNR targets, it is approximated

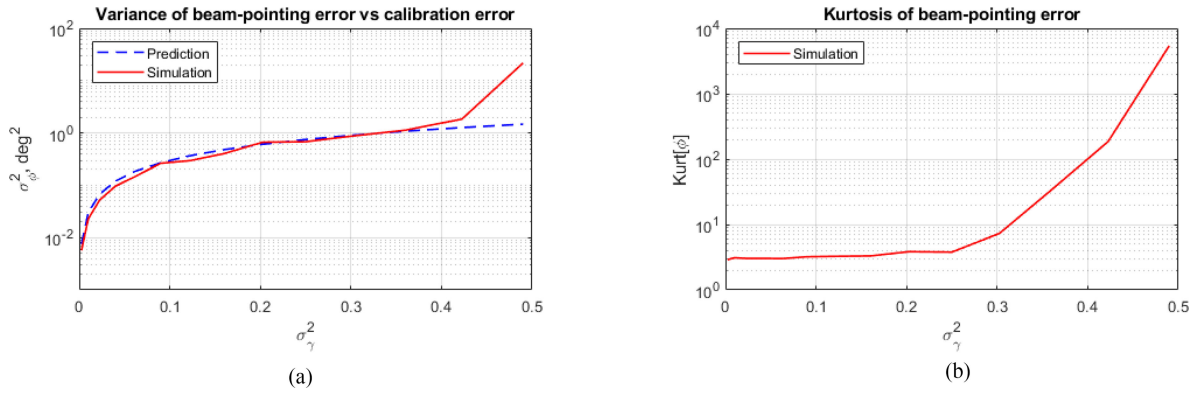


Fig. 2. Beam-pointing error standard deviation (a) and kurtosis (b) of bearing estimation with a linear array vs calibration error  $\sigma_{\gamma}^2$ ,  $M = 12$ ,  $\phi = 0$ .

by Cramer-Rao bound [25]:

$$\sigma_{\phi,i}^2 \geq \frac{3\lambda^2}{\pi^2 d^2 \cos^2(\phi_i)(M-1)^3 \text{SNR}}. \quad (44)$$

When the bearing estimation (41) is substituted by (40), the state vector is amended with a new map feature. The parts of the mean square error (MSE) matrix  $\hat{\mathbf{M}}^{[t]}$  that characterise the landmark location uncertainty and its correlation to the platform location uncertainty are:

$$\mathbf{M}_{i,i} = \mathbf{J}_x \mathbf{M}_x \mathbf{J}_x^T + \mathbf{J}_{\tilde{\mathbf{z}}} \tilde{\mathbf{R}}_i \mathbf{J}_{\tilde{\mathbf{z}}}^T; \quad (45)$$

$$\mathbf{M}_{i,x} = \mathbf{J}_x \mathbf{M}_x; \quad (46)$$

$$\mathbf{M}_{i,m} = \mathbf{J}_x \mathbf{M}_{x,m}, \quad (47)$$

where  $\mathbf{M}_x \in \mathbb{R}^{1:4,1:4}$  defines the uncertainty of the platform location and  $\mathbf{J}_x \in \mathbb{R}^{2 \times 4}$  stands for the Jacobian of the landmark coordinates (40) with respect to  $\mathbf{x}^{[t]}$ . For the landmark initialisation we introduce a modified measurement vector  $\tilde{\mathbf{z}}_i = [r_i, v_{r,i}, \phi_i]^T$ , with  $\phi_i$  being estimated by (41). The covariance matrix of the observation noise therefore becomes:  $\tilde{\mathbf{R}}_i = \text{diag}[\sigma_{r,i}^2, \sigma_{v,i}^2, \sigma_{\phi}^2]$ . The Jacobian of the modified measurements  $\mathbf{J}_{\tilde{\mathbf{z}}} \in \mathbb{R}^{2 \times 3}$  is derived from (40). The cross-covariance between the new feature and the sensor location is defined by submatrix  $\mathbf{M}_{i,x}$ , and that between the new feature and the map is defined by  $\mathbf{M}_{i,m}$ . Since matrix  $\mathbf{M}$  is symmetric,  $\mathbf{M}_{x,i} = \mathbf{M}_{i,x}^T$  and  $\mathbf{M}_{m,i} = \mathbf{M}_{i,m}^T$ .

It is important to note here that for the SLAM using range/bearing/Doppler measurements, the variance of the angular measurements can be predicted similarly by (42) and incorporated in the measurement error. This, however, does not provide self-calibration capability.

#### D. Dynamic Model

The prediction of the state and its covariance is made based on the dynamic model of the moving platform. Compared to the standard SLAM techniques, the state vector encompasses the calibration coefficients of the whole array. For the calibration coefficients we consider the dynamic model:

$$\gamma_{m,t}^R = \gamma_{m,t-1}^R + w_{m,t}^R; \quad (48)$$

$$\gamma_{m,t}^I = \gamma_{m,t-1}^I + w_{m,t}^I; \quad (49)$$

where  $w_m^R, w_m^I \sim \mathcal{N}(0, \sigma_w^2)$  and  $\sigma_w \in [10^{-6}, 10^{-3}]$ . Note that with  $\sigma_w^2 \rightarrow 0$ , Kalman filter for calibration converges to the least squares solution (6).

#### E. Applicability and Convergence

Below is a summary of the three assumptions we made when deriving the proposed technique for joint SLAM and calibration:

- 1) All landmarks are considered stationary. The responses of moving targets can be filtered out by removing from the detection list the targets not satisfying  $|\bar{v} - v_{r,i} / \cos(\phi_i)| \leq \epsilon_v$ , where  $\bar{v}$  is the predicted velocity of the platform and  $\epsilon_v$  is the acceptable tolerance;
- 2) The data association problem is correctly resolved [28];
- 3) The calibration error is dominated by the amplitude and phase errors in the channels, while the impact of coupling is small. It can be modeled by Gaussian distribution and is homogeneous over the channels. This gives rise to (43) applicable to an equispaced array with  $\lambda/2$  spacing and  $M = 12$  for  $\sigma_{\gamma} \leq 0.4$ .

The convergence of SLAM techniques, especially EKF-SLAM, has been widely investigated. No explicit conditions for EKF-SLAM convergence are declared in the literature. It has been noticed that the main source of its time inconsistency is the heading error, induced by the control command of the vehicle [31]. The proposed method addresses this problem in two ways. First, the Doppler/angular relationship can be used to accurately estimate the heading change of the vehicle. Access to Doppler measurements allows predictions to be made without the use of control commands, extracting them instead from the measured data. Second, the primary objective of calibration can be solved with a few measurements, with no need to estimate the trajectory and the map over a long period of time. This procedure of auto-calibration can be run as needed, using the previous calibration coefficients for the initialisation.

## V. SIMULATIONS

For comparison here we have modified the EKF-SLAM simulator created by Tim Balie [32], considered for performance assessment of SLAM algorithms in a few studies [31], [33], [34].

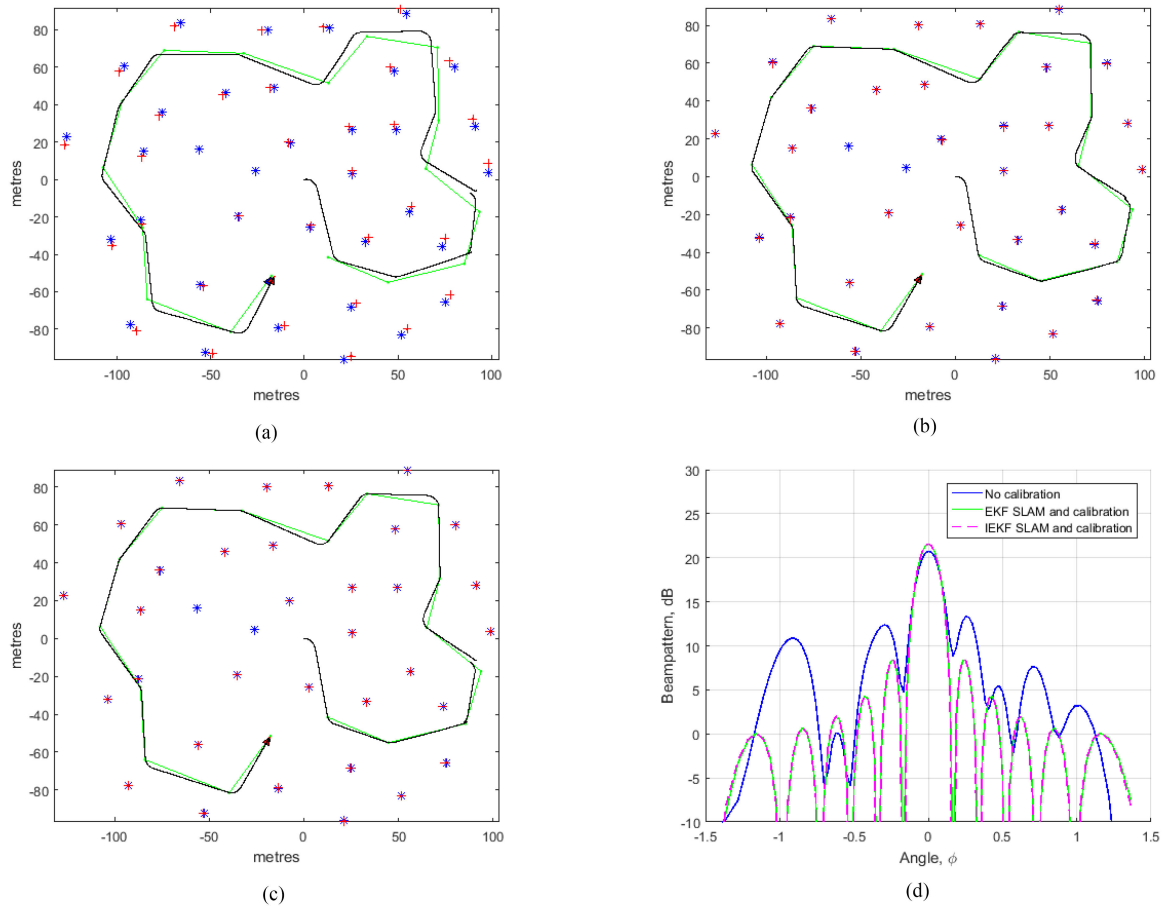


Fig. 3. Simulated map and trajectory: blue - true map and sensor locations, red - estimated map and sensor locations, green - polygon chain of the trajectory checkpoints, black - estimated trajectory: (a) SLAM with no calibration, (b) EKF-SLAM with calibration, (c) IEKF-SLAM with calibration, (d) antenna beam-pattern at the end of the simulation.

### A. Scenario

In the simulations we consider a forward-looking virtual phased array radar with  $M = 12$  elements with  $d = \lambda/2$  spacing, operating at the centre frequency  $f_c = 77$  GHz. The observation area of the radar is limited in range by  $R \leq R_{\max} = 50$  m and in angle by  $|\phi| \leq \phi_{\max} = 75^\circ$ . The platform moves with constant velocity  $v_0 = 3$  m/s, and its control inputs have Gaussian error in velocity and heading with standard deviations  $\sigma_v = 0.3$  m/s and  $\sigma_\theta = 3^\circ$ , respectively. Dynamic model of the calibration coefficients in (48) is set to  $\sigma_w = 10^{-5}$ . Calibration error follows  $\gamma_m^R \sim \mathcal{N}(1, \sigma_\gamma^2)$  and  $\gamma_m^I \sim \mathcal{N}(0, \sigma_\gamma^2)$ , with  $\sigma_\gamma = 0.3$ . For simplicity of analysis, we consider all the measurements to have the same SNR, which is rigorously incorrect but allows for a simple analysis of the calibration performance. Herein we refer to SNR in each antenna element before beamforming.

A simulation example with  $\text{SNR} = 20$  dB,  $\sigma_R = 0.5$ ,  $\sigma_{vr} = 0.5$  is shown in Fig. 3 for three cases: (a) – SLAM with no calibration, (b) – proposed algorithms realised via EKF, and (c) – realised via iterated extended Kalman filter (IEKF) [35], [36]. In IEKF the measurement update of EKF is iterated to achieve better estimation of the state variables. This makes IEKF more robust to large nonlinearities of the measurement model (31).

The results of beamforming in the direction  $\phi_0 = 0$  before calibration and with the proposed approach for auto-calibration

are given in Fig. 3(d). It is evident that appropriate calibration is essential for accurate mapping; the performance of SLAM significantly degrades with uncalibrated data, see Fig. 3(a). Note that this simulation accounts only for the increase of the bearing error as the result of poor array calibration. However, even severe degradation of SLAM performance is expected due to the appearance of false targets in the direction of a sidelobe. Note that sidelobes due to calibration error cannot be suppressed separately from calibration by applying a weighting function or adaptive beamforming.

In the following subsections, the performance of the proposed self-calibration algorithm is evaluated numerically with three metrics, tested through  $N_r = 100$  Monte-Carlo realisations with the map and platform control command, as shown in Fig. 3.

### B. Calibration Error

The first metric to be investigated is the root mean squared error (RMSE) of the calibration vector  $\gamma^{[t]}$ :

$$\text{RMSE}_{\gamma}^{[t]} = \sqrt{\frac{\sum_{n=1}^{N_r} \sum_{m=1}^{M-1} \left( \hat{\gamma}_{m,(n)}^{[t]} - \gamma_{m,(n)}^{[t]} \right)^2}{N_r (M - 1)}}, \quad (50)$$

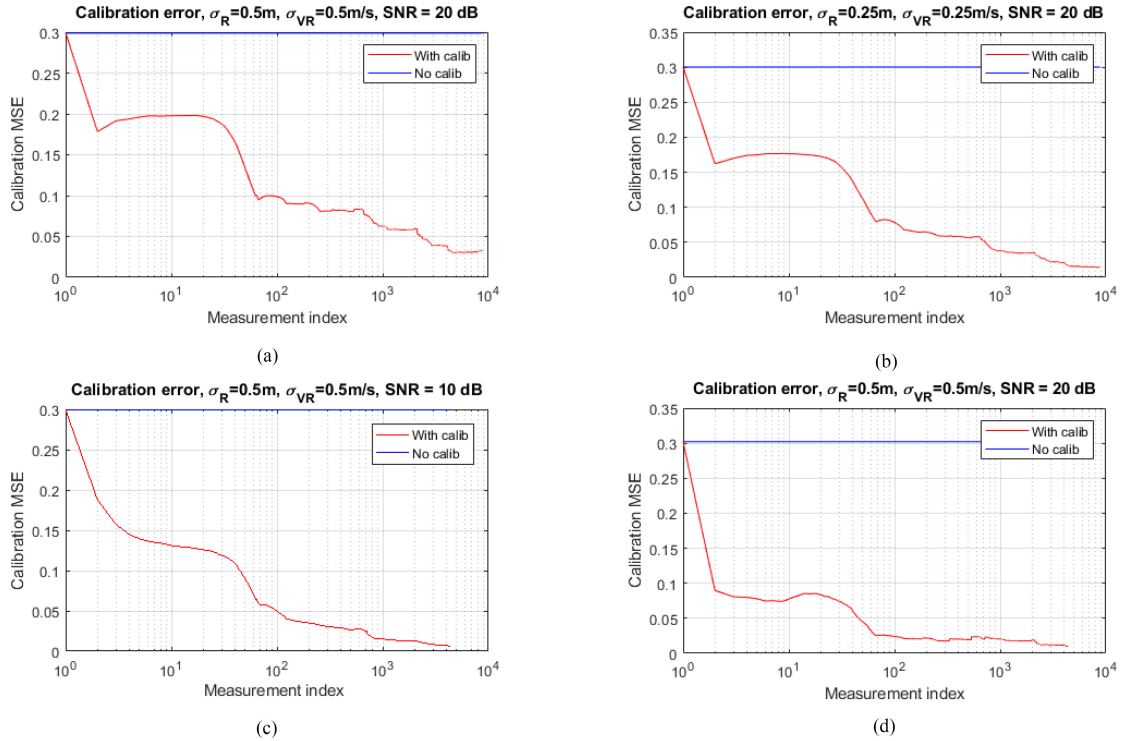


Fig. 4. Calibration error as the function of measurements: (a)  $\sigma_R = 0.5$ ,  $\sigma_v = 0.5$ , SNR = 20 dB, EKF; (b)  $\sigma_R = 0.25$ ,  $\sigma_v = 0.25$ , SNR = 20 dB, EKF; (c)  $\sigma_R = 0.5$ ,  $\sigma_v = 0.5$ , SNR = 10 dB, EKF; (d)  $\sigma_R = 0.5$ ,  $\sigma_v = 0.5$ , SNR = 20 dB, IEKF.

where the subscript notation  $(\cdot)_{(n)}$  indicates the iteration of Monte-Carlo realisation. Fig. 4 shows the simulation results for three cases with different values of SNR and range/velocity accuracy and the result of applying IEKF. These results demonstrate a small impact of range and radial velocity measurement error in the convergence of the calibration. In all of the scenarios, the estimator converges to a small calibration error:  $\sigma_\gamma < 0.05$  in less than 100 measurements. Moreover, measurements with SNR = 10 dB and an IEKF result show faster convergence. In the first few iterations, the calibration error can have nondecreasing behaviour because of the initialisation with  $\hat{\gamma} = \mathbf{1}_M$  and the presence of only a limited number of measured landmarks. The iterative procedure of IEKF (Fig. 4(d)) and larger observation noise (Fig. 4(c)) minimise this effect. In all the cases the RMSE of the calibration coefficients is smaller than that before calibration.

### C. Beam-Pointing Error

Calibration error results in biased angular measurements. To examine this we analyse the impact of the proposed auto-calibration on the beam-pointing error in the direction  $\phi_0 = 0$  (note that angular error induced by calibration (43) is minimal in the direction  $\phi_0 = 0$ ):

$$RMSE_{\phi_0}^{[t]} = \sqrt{\frac{\sum_{n=1}^{N_r} \left( \hat{\phi}_{0,(n)}^{[t]} \right)^2}{N_r}}, \quad (51)$$

with  $\hat{\phi}_{0,(n)}^{[t]}$  being the DOA estimation (41) in the direction  $\phi_0$  using the calibration vector  $\hat{\gamma}_{(n)}^{[t]}$ . The data vector for this analysis is noise-free, i.e.,  $\mathbf{p} = \mathbf{1}_M$ .

Simulation results are demonstrated in Fig. 5. As a reference, the error before calibration is also shown there. The behaviour of the beam-pointing error over time is similar to that of the calibration error. The increase in both calibration and beam-pointing error in early iterations is due to the initialisation procedure: when the radar observes all landmarks in the scene for the first time, the map is initialised according to the existing range and angular measurements, see (40), (41). The angle is measured with the standard beamforming, assuming that no calibration error exists,  $\hat{\gamma} = \mathbf{1}_M$ , i.e., the best option possible with the available data. This results in an error in the angular measurement and mapping of the target with an offset in  $(x_i, y_i)$  coordinates. In the next time instant these landmark coordinates  $(x_i, y_i)$  are used to create measurement prediction and update the state vector, including the calibration coefficients. Thus, the calibration coefficients obtained after the first few measurements represent the calibration for a biased angle: the behaviours shown in Fig. 4 and Fig. 5. The new measurements have a greater divergence from the measurement prediction, especially in Doppler velocity. The routing of EKF minimises both measurement and model dynamic errors, using the newly collected data, and this leads to the correction of the map and the minimisation of future calibration and beam-pointing errors.

### D. Sidelobe Level

The main consequence of calibration error for the array beamformer is the rise of the sidelobe level, which leads to false detections. The sidelobe level of the beamformer in the direction  $\phi_0 = 0$  is investigated. As the metric of calibration performance, the inverse of the peak-to-sidelobe ratio of the

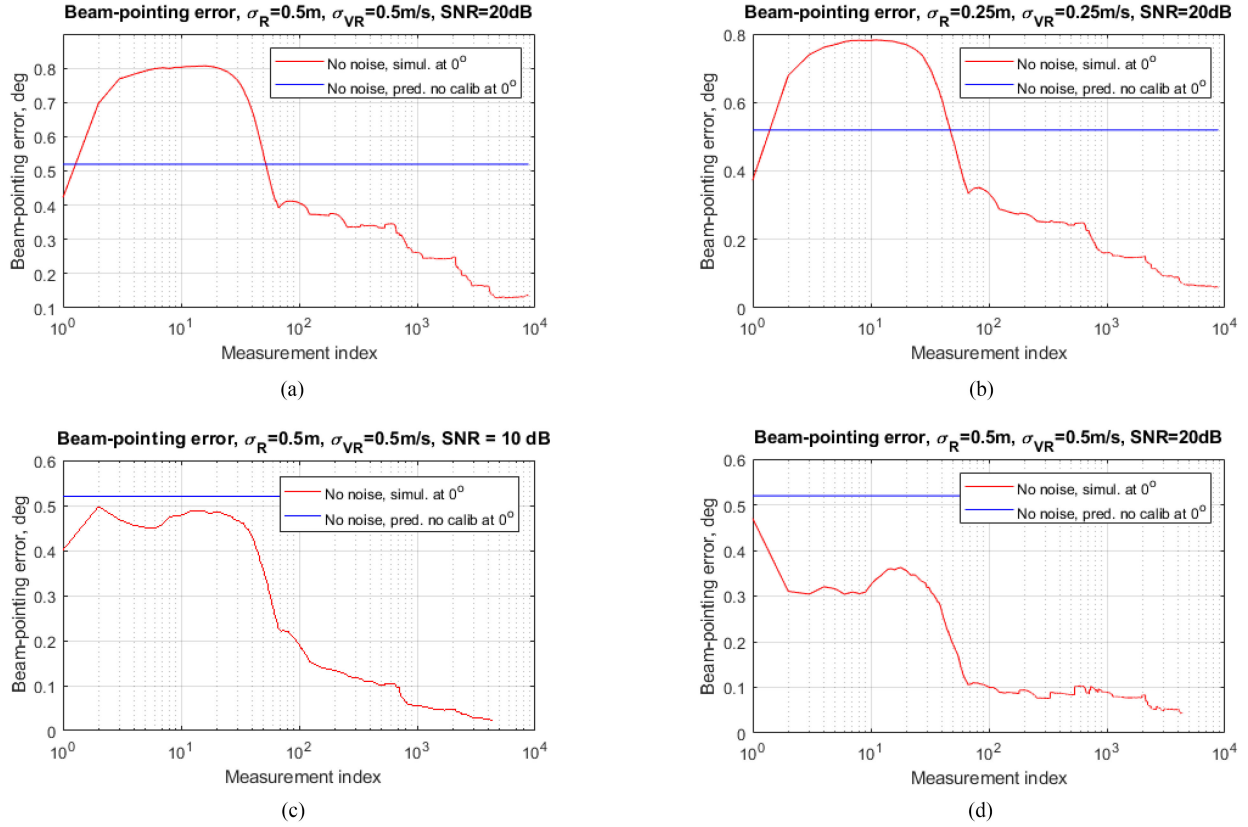


Fig. 5. Beam-pointing error in the direction  $\phi = 0$  as the function of measurements: (a)  $\sigma_R = 0.5$ ,  $\sigma_v = 0.5$ , SNR = 20 dB, EKF; (b)  $\sigma_R = 0.25$ ,  $\sigma_v = 0.25$ , SNR = 20 dB, EKF; (c)  $\sigma_R = 0.5$ ,  $\sigma_v = 0.5$ , SNR = 10 dB, EKF; (d)  $\sigma_R = 0.5$ ,  $\sigma_v = 0.5$ , SNR = 20 dB, IEKF.

standard beamformer is obtained at every realisation:

$$SL_{(n)}^{[t]} = \frac{\max_{\phi \in \Phi_{SL}} \left( \mathbf{a}^H(\phi) \left( \hat{\boldsymbol{\gamma}}_{(n)}^{[t]} \right)^{\odot -1} \right)}{\max_{\phi \in \Phi_{ML}} \left( \mathbf{a}^H(\phi) \left( \hat{\boldsymbol{\gamma}}_{(n)}^{[t]} \right)^{\odot -1} \right)}, \quad (52)$$

where  $(\cdot)^{\odot -1}$  defines the Hadamard inverse of the vector, and  $\Phi_{SL} = \{|\phi| \geq \lambda / ((M - 1)d)\}$  and  $\Phi_{ML} = \{|\phi| < \lambda / ((M - 1)d)\}$  are correspondingly the sidelobe and mainlobe intervals of the angular grid. From the measured sidelobe level at every realisation (52), we are interested in two metrics: the average sidelobe level as the function of measurements:

$$SL_{\text{mean}}^{[t]} = \frac{1}{N_r} \sum_{n=1}^{N_r} SL_{(n)}^{[t]}; \quad (53)$$

and the maximum sidelobe level (or its largest order statistic):

$$SL_{\text{max}}^{[t]} = \max_n SL_{(n)}^{[t]}. \quad (54)$$

The latter shows the worst case scenario for calibration performance over  $N_r = 100$  Monte-Carlo realisations. The results are presented together with the sidelobe level upon initialisation in Fig. 6. It can be seen that the average first sidelobe level without calibration is about  $-10$  dB, and it reaches  $-6$  dB in some realisations. The small difference between the maximum and average sidelobe levels before calibration in Fig. 6, (a)–(d) is

due to the estimation of these metrics from the limited number of Monte-Carlo trials  $N_r = 100$ .

The proposed calibration procedure reduces the average sidelobe level already after a couple of measurements to the value within 1 dB from the ideal calibration. After about 100 measurements, even the worst case scenario approaches the benchmark value of  $-13$  dB. Note that IEKF achieves the same performance after just a few measurements. These results demonstrate the efficiency of the proposed approach for antenna array self-calibration.

## VI. APPLICATION TO REAL DATA

To demonstrate the effectiveness of the proposed approach, a real data set has been collected with a commercial automotive radar, operating at 77 GHz and having 3 Tx  $\times$  4 Rx MIMO array for azimuth scanning. The radar provides 10 frames of real data per second with range resolution  $\delta_R \approx 0.16$  m and Doppler resolution  $\delta_v \approx 0.04$  m/s in one frame. In the considered scenario the car was moving with a low velocity (below 20 km/h, to avoid velocity ambiguities) over TU Delft campus. The trajectory of the car and the scene are shown in Fig. 7 and Fig. 8, respectively. The initial location of the car is set to be equal to the GPS measurement. It can be seen in Fig. 7 that the SLAM trajectory closely follows the GPS trajectory and has an offset from the centre of the road due to GPS initialisation.

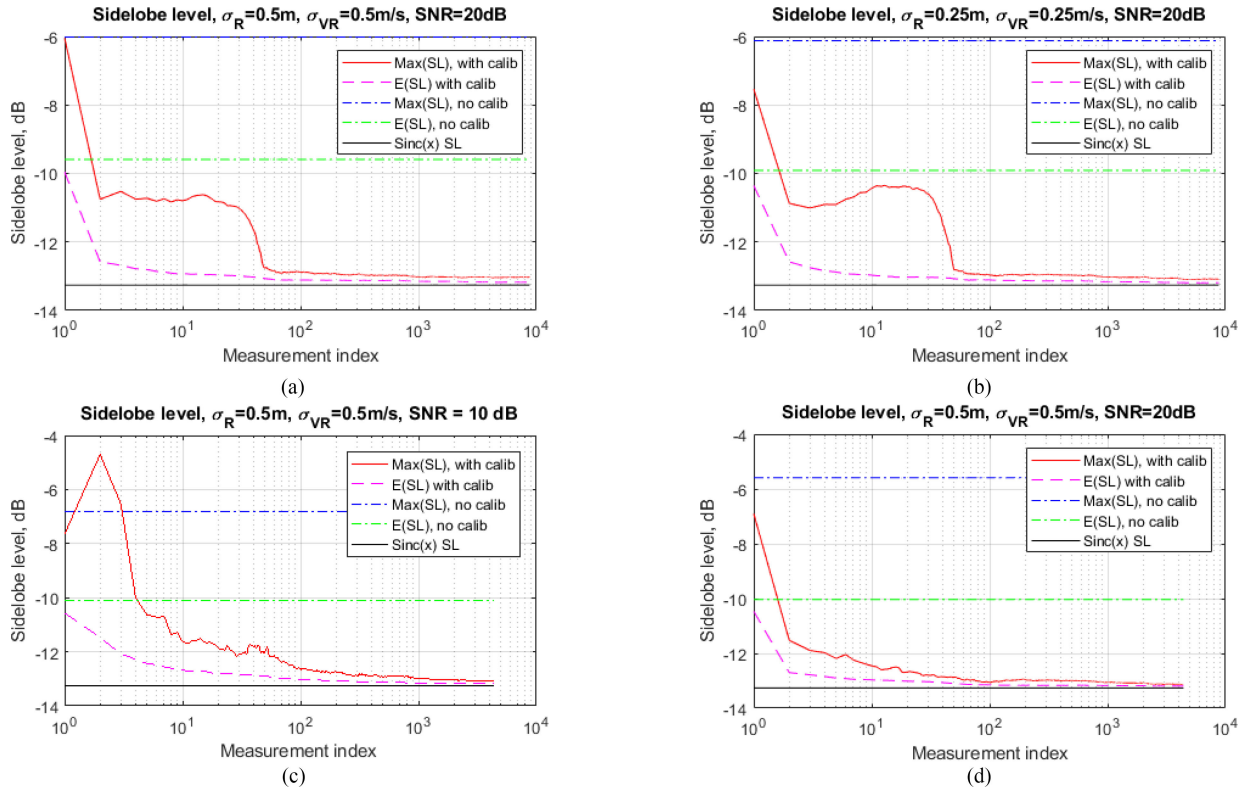


Fig. 6. Sidelobe level in the direction  $\phi = 0$  as the function of measurements: (a)  $\sigma_R = 0.5$ ,  $\sigma_v = 0.5$ , SNR = 20 dB, EKF; (b)  $\sigma_R = 0.25$ ,  $\sigma_v = 0.25$ , SNR = 20 dB, EKF; (c)  $\sigma_R = 0.5$ ,  $\sigma_v = 0.5$ , SNR = 10 dB, EKF; (d)  $\sigma_R = 0.5$ ,  $\sigma_v = 0.5$ , SNR = 20 dB, IEKF.

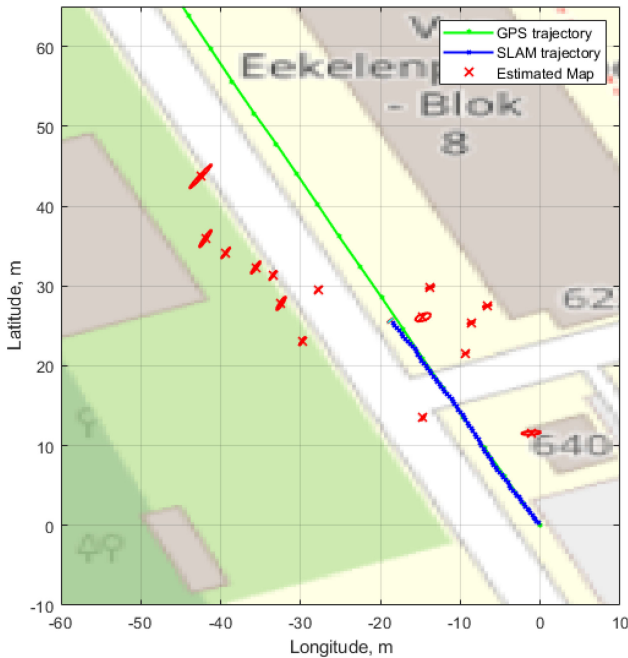


Fig. 7. The car's trajectory with GPS (green) and with SLAM (blue). The estimated map is shown in red.

To apply the proposed algorithm, we made the following preprocessing of the raw radar data. Radar delivers a data cube (slow-time/fast-time/array element) in every frame.



Fig. 8. The observed scene from the forward-looking camera.

Conventional range-Doppler-angle processing is applied, followed by a median detector. Detections in range/Doppler velocity/angle space are then grouped in agglomerative clusters with the threshold for cutting the hierarchical tree being equal to 5. Moreover, targets with outliers in Doppler velocity  $|\bar{v} - v_{r,i} / \cos(\phi_i)| > 0.3$  m/s and at angles  $\phi > 60^\circ$  are also rejected. For each cluster, only one detection with the maximum SNR is treated as a detected target. Antenna array responses of these targets are then extracted from the original data cube to get the measurement vector in the format of (13).

The calibration coefficients estimated after  $\{20, 40, 60, 80\}$  frames are demonstrated in Fig. 9(a). Already after 20 frames a good estimation of the calibration coefficients are obtained, and there is only minor variation after processing more data

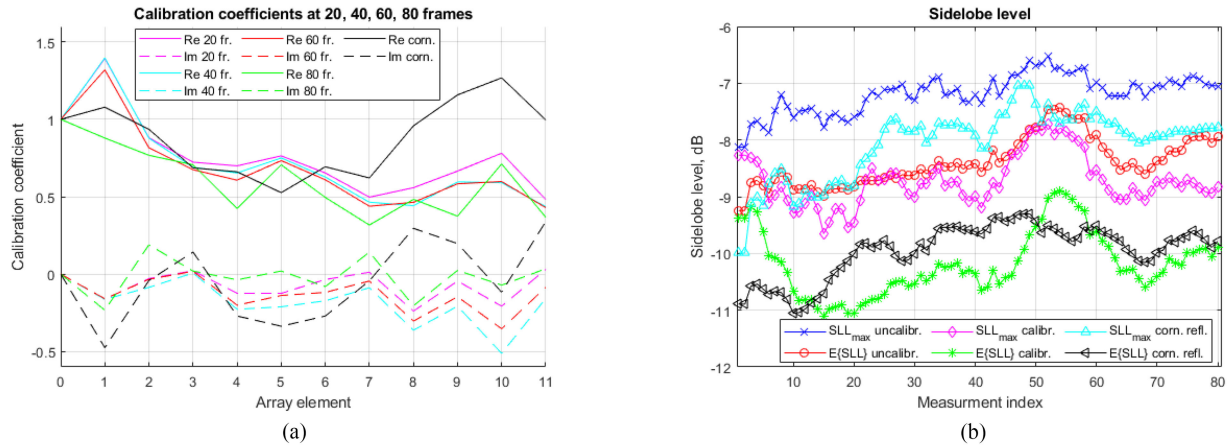


Fig. 9. (a) Estimation of calibration coefficients after 20, 40, 60, 80 frames together with calibration using a corner reflector; (b) peak-to-sidelobe level of uncalibrated array, using proposed auto-calibration and calibrated with a corner reflector.

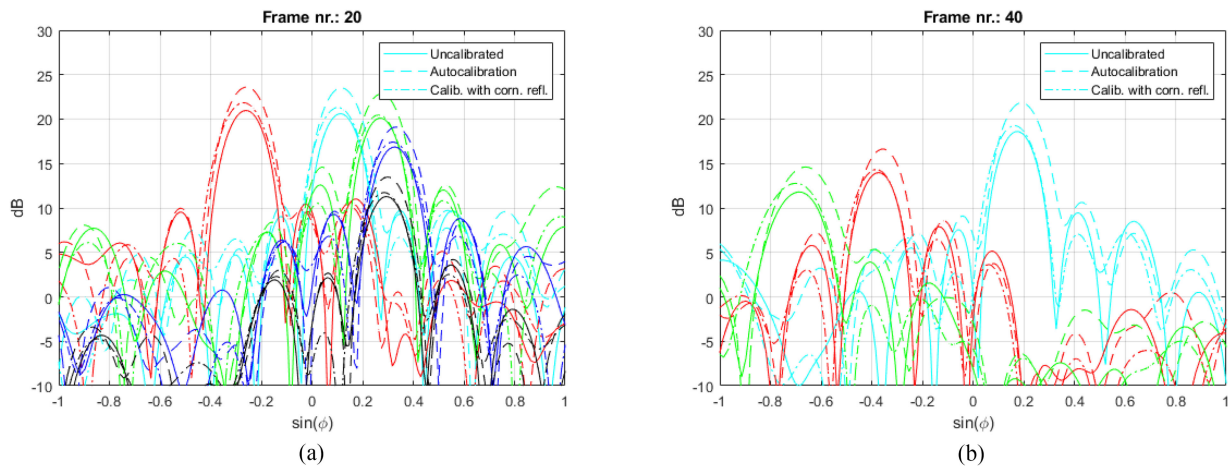


Fig. 10. Beamforming output in frames 20 (a) and 40 (b) of uncalibrated array, using the proposed auto-calibration and calibrated with a corner reflector. Different colours in each plot correspond to distinct observed landmarks.

frames. Note that the preliminary calibration of the MIMO array was made in an anechoic chamber about one year before this measurement campaign. The quality of the calibration is evaluated by analyses of the target response before and after the proposed auto-calibration, as the examples in Fig. 10 show. For comparison we added to those examples the results of the beamforming using corner reflector measurements collected on the same day (with the radar already attached to the car). A few comments should be made regarding Fig. 10: first, the target response after calibration has a higher peak-to-sidelobe level, which is mainly achieved by the rise of the main-lobe response. That is because we use  $\gamma_0 = 1$  as the constraint, rather than a constant norm of the calibration vector. Second, the peaks of the calibrated array response, both using auto-calibration and a corner reflector, look biased from the peak of the uncalibrated antenna response. That can be explained by the fact that the radar was attached to the bumper about half a metre off from the centre of the car, and also because the curvature of the bumper

made the aiming direction slightly biased from the forward direction of the auto. Also, no special tools were used to align the corner reflector with the radar line of sight, which leads to a sinusoid-like pattern of the imaginary part of the calibration coefficients for corner reflector data in Fig. 9(a). The proposed auto-calibration successfully corrects this bias, as shown by the imaginary part of calibration coefficients in Fig. 9(a).

Finally, the quality of the calibration is evaluated by the analysis of the average sidelobe level (53) and the maximum sidelobe level (54) in every frame. These results are shown in Fig. 9(b) by the moving average window over 5 frames. The results demonstrate that both calibration with a corner reflector and the proposed auto-calibration improves the average and the peak sidelobe levels by approximately 2 dB compared to an uncalibrated array. Note that for this we analyse the sidelobes for beamforming in the direction of the target, and not for  $\phi_0 = 0$  as it was in Section V, which raises the levels of  $SL_{\text{mean}}^{[t]}$  and  $SL_{\text{max}}^{[t]}$ .

## VII. CONCLUSION

In this paper we have addressed the problem of how to continuously calibrate a forward-looking phased array radar under operational conditions. It was shown that the dynamic calibration of automotive radar using targets of opportunity requires the joint solution of sensor localisation, mapping and calibration. For the first time, the probabilistic formulation of the joint localisation, mapping and calibration was derived and an extended Kalman filter-based solution to the problem was proposed. The problem of target initialisation in the presence of calibration errors was discussed. The proposed approach can compensate for moderate amplitude and phase errors in the calibration vector (with standard deviation up to 40% of the mean value) and provides a means for the reliable estimation of calibration coefficients after processing a few tens of measurements. The improvement achieved by solving the joint problem was demonstrated via numerical simulations and the analysis of real data records. In particular, compensation of the radar steering bias and 2 dB improvement in sidelobe level suppression was shown with the application of the proposed approach to the real data. Utilisation of more advanced scattering models for the landmarks represented by extended targets may further improve the accuracy of the calibration procedure.

## ACKNOWLEDGMENT

The authors thank Fred van der Zwan, Peter Swart and Pascal Aubry for their help with the radar measurements and Lisa Audenaert for the simulations made during the study.

## REFERENCES

- [1] J. Dickmann *et al.*, "Automotive radar the key technology for autonomous driving: From detection and ranging to environmental understanding," in *Proc. IEEE Radar Conf.*, 2016, pp. 1–6.
- [2] M. Viberg, M. Lanne, and A. Lundgren, "Calibration in array processing," in *Classical Modern Direction-Arrival Estimation*. Elsevier, 2009, pp. 93–124.
- [3] K. Carver, W. Cooper, and W. Stutzman, "Beam-pointing errors of planar phased arrays," *IEEE Trans. Antennas Propag.*, vol. 21, no. 2, pp. 199–202, Mar. 1973.
- [4] B. Friedlander, "Sensitivity analysis of the maximum likelihood direction-finding algorithm," *IEEE Trans. Aerosp. Electron. Syst.*, vol. 26, no. 6, pp. 953–968, Nov. 1990.
- [5] B. Porat and B. Friedlander, "Accuracy requirements in off-line array calibration," *IEEE Trans. Aerosp. Electron. Syst.*, vol. 33, no. 2, pp. 545–556, Apr. 1997.
- [6] R. A. Monzingo and T. W. Miller, *Introduction to Adaptive Arrays*. Raleigh, N.C.: Scitech, 2004.
- [7] A. J. Weiss and B. Friedlander, "Eigenstructure methods for direction finding with sensor gain and phase uncertainties," *Circuits, Syst. Signal Process.*, vol. 9, no. 3, pp. 271–300, 1990.
- [8] B. C. Ng and C. M. S. See, "Sensor-array calibration using a maximum-likelihood approach," *IEEE Trans. Antennas Propag.*, vol. 44, no. 6, pp. 827–835, Jun. 1996.
- [9] M. Lanne, M. Viberg, and A. Lundgren, "Adaptive beamforming using calibration vectors with unknown gain and phase," in *Proc. IEEE Antennas Propag. Soc. Int. Symp.*, 2007, pp. 4208–4211.
- [10] A. J. Weiss and B. Friedlander, "Array shape calibration using sources in unknown locations—a maximum likelihood approach," *IEEE Trans. Acoust., Speech, Signal Process.*, vol. 37, no. 12, pp. 1958–1966, Dec. 1989.
- [11] Y. Rockah and P. Schultheiss, "Array shape calibration using sources in unknown locations—Part I: Far-field sources," *IEEE Trans. Acoust., Speech, Signal Process.*, vol. 35, no. 3, pp. 286–299, Mar. 1987.
- [12] M. Levi and H. Messer, "Sufficient conditions for array calibration using sources of mixed tapes," in *Proc. IEEE Int. Conf. Acoust., Speech, Signal Process.*, 1990, pp. 2943–2946.
- [13] A. Flieller, A. Ferréol, P. Larzabal, and H. Clergeot, "Robust bearing estimation in the presence of direction-dependent modelling errors: Identifiability and treatment," in *Proc. Int. Conf. Acoust., Speech, Signal Process.*, 1995, vol. 3, pp. 1884–1887.
- [14] L. Qiong, G. Long, and Y. Zhongfu, "An overview of self-calibration in sensor array processing," in *Proc. 6th Int. Symp. Antennas, Propag. EM Theory 2003*, pp. 279–282.
- [15] S. Xu, B. J. Kooij, and A. Yarovsky, "Joint doppler and DOA estimation using (ultra-) wideband FMCW signals," *Signal Process.*, vol. 168, p. 107259, 2020. [Online]. Available: <https://www.sciencedirect.com/science/article/pii/S0165168419303111>
- [16] V. Cevher and J. H. McClellan, "Sensor array calibration via tracking with the extended Kalman filter," in *Proc. IEEE Int. Conf. Acoust., Speech, Signal Process.*, 2001, vol. 5, pp. 2817–2820.
- [17] J. Pierre and M. Kaveh, "Experimental performance of calibration and direction-finding algorithms," in *Proc. IEEE Int. Conf. Acoust., Speech, Signal Process.*, 1991, pp. 1365–1368.
- [18] C. M. Schmid, C. Pfeffer, R. Feger, and A. Stelzer, "An FMCW MIMO radar calibration and mutual coupling compensation approach," in *Proc. IEEE Eur. Radar Conf.*, 2013, pp. 13–16.
- [19] F. Belfiori, W. van Rossum, and P. Hoogeboom, "Array calibration technique for a coherent MIMO radar," in *Proc. 13th Int. Radar Symp.*, 2012, pp. 122–125.
- [20] M. Harter, A. Ziroff, J. Hildebrandt, and T. Zwick, "Error analysis and self-calibration of a digital beamforming radar system," in *Proc. IEEE MTT-S Int. Conf. Microw. Intell. Mobility*, 2015, pp. 1–4.
- [21] M. Harter, J. Hildebrandt, A. Ziroff, and T. Zwick, "Self-calibration of a 3-D-digital beamforming radar system for automotive applications with installation behind automotive covers," *IEEE Trans. Microw. Theory Techn.*, vol. 64, no. 9, pp. 2994–3000, Sep. 2016.
- [22] J. Domhof, R. Happee, and P. Jonker, "Multi-sensor object tracking performance limits by the cramer-rao lower bound," in *Proc. 20th Int. Conf. Inf. Fusion*, 2017, pp. 1–8.
- [23] "ADAS TEXAradar and camera calibration solutions," Accessed: Apr. 14, 2020. [Online]. Available: <https://www.texa.com/products/radar-camera-calibration-kit>
- [24] "DAS Bosch1000 calibration set: Professional adjustment of sensors and cameras of driver assistance systems," Accessed: Apr. 14, 2020. [Online]. Available: <https://www.bosch-presse.de/pressportal/de/en/bosch-das-1000-calibration-set-professional-adjustment-of-sensors-and-cameras-of-driver-assistance-systems-151808.html>
- [25] S. M. Kay, *Fundamentals of Statistical Signal Processing, Volume I: Estimation Theory*. Englewood Cliffs, NJ, USA: Prentice Hall, 1993.
- [26] H. Durrant-Whyte and T. Bailey, "Simultaneous localization and mapping: Part I," *IEEE Robot. Automat. Mag.*, vol. 13, no. 2, pp. 99–110, Jun. 2006.
- [27] T. Bailey and H. Durrant-Whyte, "Simultaneous localization and mapping (SLAM): Part II," *IEEE Robot. Automat. Mag.*, vol. 13, no. 3, pp. 108–117, Sep. 2006.
- [28] S. Thrun, W. Burgard, and D. Fox, vol. 1, *Probabilistic Robotics*. Cambridge, MA, USA: MIT Press, 2000.
- [29] G. Bresson, Z. Alsayed, L. Yu, and S. Glaser, "Simultaneous localization and mapping: A survey of current trends in autonomous driving," *IEEE Trans. Intell. Veh.*, vol. 2, no. 3, pp. 194–220, Sep. 2017.
- [30] D. H. Dini and D. P. Mandic, "Class of widely linear complex kalman filters," *IEEE Trans. Neural Netw. Learn. Syst.*, vol. 23, no. 5, pp. 775–786, May 2012.
- [31] T. Bailey, J. Nieto, J. Guivant, M. Stevens, and E. Nebot, "Consistency of the EKF-SLAM algorithm," in *Proc. IEEE/RSJ Int. Conf. Intell. Robots Syst.*, 2006, pp. 3562–3568.
- [32] T. Bailey, "SLAM package of tim bailey." [Online]. Available: <https://openslam-org.github.io/bailey-slam.html>
- [33] T. Bailey, J. Nieto, and E. Nebot, "Consistency of the FastSLAM algorithm," in *Proc. IEEE Int. Conf. Robot. Automat.*, 2006, pp. 424–429.
- [34] F. Zhang, S. Li, S. Yuan, E. Sun, and L. Zhao, "Algorithms analysis of mobile robot SLAM based on kalman and particle filter," in *Proc. IEEE 9th Int. Conf. Modelling, Identification Control.*, 2017, pp. 1050–1055.
- [35] J. Havlík and O. Straka, "Performance evaluation of iterated extended kalman filter with variable step-length," in *Proc. J. Phys.: Conf. Ser.*, vol. 659, no. 1. IOP Publishing, 2015, Art. no. 0 12022.
- [36] A. H. Jazwinski, *Stochastic Processes and Filtering Theory*. Menola, New York: Dover Publication Inc., 2007.



**Nikita Petrov** received the Engineering degree in radio-electronic control systems from Baltic State Technical University “VOENMEH” D.F. Ustinov, Saint Petersburg, Russia, in 2012 and the Ph.D. degree in radar signal processing from the Delft University of Technology, Delft, The Netherlands, in 2019. Since then, he has been a Postdoctoral Researcher with the Microwave Sensing, Signals and Systems Section, Faculty of Electrical Engineering, Mathematics, and Computer Science, Delft University of Technology.

His research interests include modern radar technologies, radar signal processing, multichannel and multiband signals and systems, high resolution, and automotive radars. He is currently a Reviewer of the *IEEE TRANSACTIONS ON AEROSPACE AND ELECTRONIC SYSTEMS* and the *IEEE TRANSACTIONS ON GEOSCIENCE AND REMOTE SENSING*.



**Oleg Krasnov** received the M.S. degree in radio physics from Voronezh State University, Voronezh, Russia, in 1982 and the Ph.D. degree in radio technique from National Aerospace University “Kharkiv Aviation Institute,” Kharkiv, Ukraine, in 1994. In 1999, he joined the International Research Center for Telecommunications and Radar, Delft University of Technology, Delft, The Netherlands. Since 2009, he has been a Senior Researcher with the Microwave Sensing, Signals and Systems Section, Faculty of Electrical Engineering, Mathematics, and Computer

Science, Delft University of Technology, where he became a Universitair Docent (Assistant Professor) in 2012. He has authored or coauthored more than 120 scientific or technical papers and holds a few patents. His research interests include radar waveforms, signal and data processing algorithms for polarimetric radars and distributed radar systems, multisensor atmospheric remote sensing, and optimal resource management of adaptive radar sensors and distributed systems. He was the Secretary of the 9th European Radar Conference (EuRAD12), Amsterdam, The Netherlands, as the Organizer and a Technical Program Committee Member of the annual International Specialist Meetings “Electromagnetic Waves and Wind Turbines,” as the Technical Program Committee Member and a Reviewer of many international radar conferences.



**Alexander G. Yarovoy** (Fellow, IEEE) received the Diploma (with hon.) in radiophysics and electronics from Kharkov State University, Kharkiv, Ukraine, in 1984, and the Candidate Physics & Mathematics Sciences and Doctor Physics & Mathematics Sciences degrees in radiophysics in 1987 and 1994, respectively. In 1987, he was a Researcher with the Department of Radiophysics, Kharkov State University, where in 1997, he became a Full Professor. From September 1994 to 1996, he was a Visiting Researcher with the Technical University of Ilmenau, Ilmenau,

Germany. Since 1999, he has been with the Delft University of Technology, Delft, The Netherlands. Since 2009, he has been the Chair of Microwave Sensing, Systems and Signals. He has authored or coauthored more than 450 scientific or technical papers, six patents, and 14 book chapters. His main research interests include high-resolution radar, microwave imaging, and applied electromagnetics (in particular, UWB antennas). He was the recipient of the European Microwave Week Radar Award for the paper that best advances the state-of-the-art in radar technology in 2001 (together with L.P. Ligthart and P. van Genderen) and in 2012 (together with T. Savelyev). In 2010, together with D. Caratelli, he was the recipient of the Best Paper Award of the Applied Computational Electromagnetic Society. He was the Chair and the Technical Program Committee Chair of the 5th European Radar Conference (EuRAD’08), Amsterdam, The Netherlands, and the Secretary of the 1st European Radar Conference (EuRAD’04), Amsterdam, The Netherlands. He was also the Co-Chair and the Technical Program Committee Chair of the Xth International Conference on GPR (GPR2004) in Delft, The Netherlands. From 2011 to 2018, he was an Associate Editor for the *International Journal of Microwave and Wireless Technologies* and the Guest Editor of five special issues of the *IEEE Transactions* and other journals. From 2008 to 2017, he was the Director of the European Microwave Association.